Two-dimensional simulation of an oxy-acetylene torch diamond reactor with a detailed gas-phase and surface mechanism

Two-dimensional simulation of an oxy-acetylene torch diamond reactor with a detailed gas-phase and surface mechanism

M. Okkerse, C. R. Kleijn,[a] and H. E. A. van den Akker
Kramers Laboratorium voor Fysische Technologie, Delft University of Technology, Prins Bernhardlaan 6, 2628 BW Delft, The Netherlands

M. H. J. M. de Croon
Laboratorium voor Chemische Technologie, Eindhoven University of Technology, Postbus 513, 5600 MB Eindhoven, The Netherlands

G. B. Marin
Laboratorium voor Petrochemische Techniek, University of Ghent, Krijgslaan 281, B-9000 Gent, Belgium

(Received 19 January 2000; accepted for publication 13 July 2000)

A two-dimensional model is presented for the hydrodynamics and chemistry of an oxy-acetylene torch reactor for chemical vapor deposition of diamond, and it is validated against spectroscopy and growth rate data from the literature. The model combines the laminar equations for flow, heat, and mass transfer with combustion and deposition chemistries, and includes multicomponent diffusion and thermodiffusion. A two-step solution approach is used. In the first step, a lumped chemistry model is used to calculate the flame shape, temperatures and hydrodynamics. In the second step, a detailed, 27 species / 119 elementary reactions gas phase chemistry model and a 41 species / 67 elementary reactions surface chemistry model are used to calculate radicals and intermediates concentrations in the gas phase and at the surface, as well as growth rates. Important experimental trends are predicted correctly, but there are some discrepancies. The main problem lies in the use of the Miller–Melius hydrocarbon combustion mechanism for rich oxy-acetylene flames. [J. A. Miller and C. F. Melius, Combustion and Flame **91**, 21 (1992)]. Despite this problem, some aspects of the diamond growth process are clarified. It is demonstrated that gas-phase diffusion limitations play a minor role in the diamond growth process, which is determined by surface kinetics. Except for atomic hydrogen, gas phase diffusion is also of minor importance for the transport of species in and behind the flame front. Finally, it is shown that penetration of nitrogen from the ambient air into the flame cannot explain the observed changes at the center of the diamond films as reported in the literature. © *2000 American Institute of Physics.* [S0021-8979(00)06420-3]

I. INTRODUCTION

The combination of computational fluid dynamics (CFD) and detailed chemistry modeling has furthered our understanding of chemical vapor deposition (CVD) processes. If complex interactions occur, experiments in themselves cannot always explain the behavior of the system. For conventional thermal CVD processes, where gas-phase and surface reactions do not release significant amounts of heat, it has proved possible to design a reactor with the aid of CFD. For example, in low pressure tungsten CVD, simulations have been used to explain and predict the influence of changes in process conditions and reactor geometry to selectivity loss.[1] However, when gas-phase reactions are highly exothermal, such as in combustion CVD, they influence the temperature profile and thus the velocity profile. Consequently, species concentrations, temperature, and flow are strongly coupled. This complicates matters significantly. The modeling of combustion CVD combines the difficulties encountered in laminar flame simulations with those of classical thermal CVD modeling.

In the field of laminar flame simulations, two approaches can be distinguished: study of detailed combustion chemistry with the aid of zero- or one-dimensional hydrodynamic models,[2,3] and flow and flame investigations with the aid of two-dimensional (2D) hydrodynamic simulations, using simple, lumped chemistry.[4–6]

Recently, for methane–air flames, these approaches have started to come together Several groups have simulated premixed 2D methane–air flames with detailed chemistry.[7–9] Somers and de Goey[7] applied the so-called skeletal reaction mechanism for methane combustion, consisting of 25 reactions and 15 species.[10] An unstructured grid, locally refined near the flame front, was used for the numerical simulations. Multicomponent diffusion phenomena were modeled in a highly simplified way, assuming a constant Lewis number for each diffusing species, and thermodiffusion was neglected. The model predictions were verified by comparing the predicted shape of the flame to experimental observations. Zhou *et al.*[8] used a 29-reaction, 13-species combustion mechanism based on Tsataronis.[11] Diffusion was again modeled with the simplified constant Lewis number approximation. Simulated concentration profiles of several stable species and of the OH radical were compared to Raman–LIF

[a]Author to whom correspondence should be addressed; electronic mail: crkleijn@klft.tn.tudelft.nl

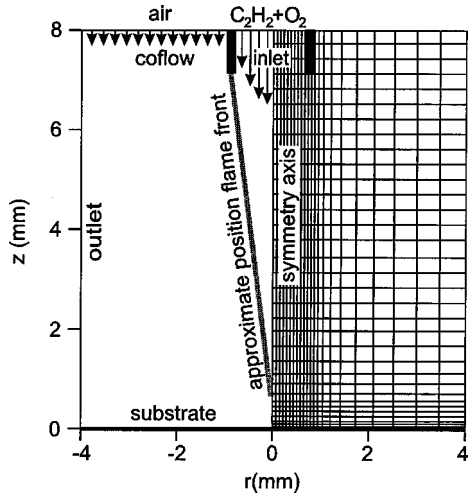

FIG. 1. Computational grid for the two-dimensional reactor model. One in every three lines is depicted horizontally and vertically.

measurements. Ern and Giovangigli[9] simulated the flame in the most detail. They made use of a 46-reaction, 16-species kinetic mechanism, and fully included multicomponents and thermodiffusion. No comparisons to experimental data were reported.

The aim of the present work is to model an oxy-acetylene flame CVD reactor for the deposition of diamond layers. The reactor consists of an ordinary welding torch, pointed toward a cooled substrate (see Fig. 1). The torch is fed with acetylene and oxygen, with an amount of acetylene slightly above the amount needed to form a neutral flame. The rich flame burns to CO and H_2, in contrast to a flame that burns to CO_2, which is generally defined to be stoichiometric. Due to the high flame temperature and the carbon excess, carbon radicals are formed, causing the growth of diamond on the substrate. No full 2D simulations have been reported for acetylene–oxygen flames. These flames have higher flame speeds and adiabatic flame temperatures than methane–air flames. This, combined with the larger number of species and reactions necessary to correctly model the combustion chemistry, makes the problem more complex. In the present study, the simulation of the oxy-acetylene flame is of secondary interest. The primary interest is in a correct description of the diamond growth process, by combining: (1) a detailed combustion mechanism and (2) a detailed diamond growth mechanism with (3) 2D CFD.

The starting point for our combustion mechanism was the hydrocarbon combustion mechanism by Miller and Melius,[12] which consists of 48 species and 219 reactions. This model was successfully used for the simulation of oxy-acetylene flames by Meeks *et al.*[13] For a rich flame with a C_2 fuel, the mechanism cannot be reduced to the same size as for lean methane–air flames. In a previous study,[14] we reduced the mechanism to one consisting of 27 species and 119 reactions. This reduced mechanism is used in the present study.

The applied detailed surface mechanism for the growth of diamond was constructed and tested earlier.[14,15] Diamond growth occurs because a free site is created on the hydrogen covered surface, where a carbon containing gas-phase species can adsorb. After several surface reactions and reactions with gas-phase molecules, it is included in the diamond lattice. The surface mechanism used contains CH_3 and C_2H_2 as growth species, and atomic hydrogen, and atomic and molecular oxygen as species that remove molecules from the surface. In the surface mechanism, the species are randomly distributed over the surface. Detailed Monte Carlo simulations, accounting for nonrandom distribution of species on the surface, are beginning to be employed fruitfully,[16–18] but require lengthy computation times. Moreover, recent Monte Carlo simulations[17] show that multicarbon clusters are rare on the (100) surface, thus justifying the assumption of the random distribution of species.

In the present article, we combine the above combustion and diamond growth models with 2D hydrodynamic flame simulations, based on the simultaneous numerical solution of the 2D axisymmetric conservation equations for mass, momentum thermal energy and chemical species. A two-step solution approach is used. In the first step, a lumped chemistry model is used to calculate the flame shape, temperatures and hydrodynamics. In the second step, the detailed gas phase chemistry and surface chemistry models are used to calculate radicals and intermediates concentrations in the gas phase and at the surface, as well as growth rates. The studied geometry is modeled after the reactor used by Klein-Douwel *et al.*[19] and is schematically depicted in Fig. 1. Simulated radial and axial concentration profiles are compared to qualitative LIF measurements and to quantitative CH measurements from the literature.

II. NUMERICAL MODEL

Simulation of the oxy-acetylene torch reactor involves the simulation of a laminar reacting flow including surface reactions. Unlike those of classical thermal CVD processes, the flow, species and heat equations are strongly coupled. As a result, the numerical equations that result from the discretization of the model equations are stiff, and their numerical solution is complicated. A description of the solution procedure is given in Sec. II A–D.

A. Equations

The simulation is based on the continuum assumption, since the mean free path under the studied conditions is on the order of 1 μm, and the flame–sheet thickness is on the order of 100 μm. Furthermore the flow can be assumed to be laminar. Although the Reynolds number is high ($\sim$7000) in the outlet of the tapered burner nozzle, no signs of turbulence are observed experimentally. This is probably caused by: (i) the short time available for onset of turbulence in the nozzle and (ii) the stabilizing effect of the flame. In fact, the nozzle is specifically designed to create laminar flames.

Under these conditions, the continuum conservation equations of mass, momentum, thermal energy and chemical species can be used to describe the system.[20] The general appearance of the transport equations for variable ϕ is given by

$$\frac{\partial \rho \phi}{\partial t} = -\nabla \cdot (\rho \mathbf{v} \phi) + \nabla \cdot (\Gamma_\phi \nabla \phi) + S_\phi^0 + S_\phi' \phi. \quad (1)$$

Here, ρ is the gas density, $\mathbf{v}$ the velocity vector, ϕ the variable to be solved, Γ_ϕ its generalized diffusion coefficient, and $S_\phi = S_\phi^0 + S_\phi' \phi$ its generalized source term, linearized in ϕ. This equation is formulated for ϕ equal to the radial velocity v_r, the axial velocity v_z, the thermal energy $c_p T$, and the N species mass fractions ω_i. The equations can further be simplified by the following assumptions: (i) the process is stationary in time; (ii) the gas behaves as a Newtonian fluid; (iii) buoyancy forces are negligible since the Grashof number is on the order of 10^{-2}; (iv) the flame is axisymmetric, i.e., there are no gradients and velocities in the tangential direction; (v) pressure effects in the thermal-energy equation are small, since relative pressure differences in the flame are on the order of 1%; (vi) transport of heat as a result of concentration gradients (the Dufour effect) can be neglected;[9] and (vii) the absorption or emission of radiation energy does not influence the temperature profile significantly.[13]

The molecular transport properties of single components, i.e., the viscosity, thermal conductivity and binary diffusion coefficient, are obtained from kinetic gas theory,[20–22] using Lennard-Jones parameters. The equation-of-state is given by the perfect gas law. The mixture viscosity and thermal conductivity can be calculated using the semiempirical averaging equations given by Reid and Sherwood.[22] The thermodynamic properties are obtained from the Chemkin thermodynamic database.[23] Multicomponent diffusion is modeled through the Wilke approximation.[24] In order to ensure mass conservation, all species fluxes except one are calculated in this way. The remaining species, with the largest mass fraction, is calculated from the constraint that all diffusion fluxes should sum up to zero.

Species diffusion driven by temperature gradients, or thermodiffusion, is often neglected in flame simulation. However, thermodiffusion generally is important if there are large differences in the size of molecules or steep temperature gradients. Both conditions apply in laminar flames. Indeed, preliminary one-dimensional flame simulations showed that if thermodiffusion is neglected, deviations are found near the flame front and near the substrate, where errors up to about 25% in the predicted species concentrations are observed. Therefore, thermodiffusion was accounted for using the Clark Jones approximation for multicomponent thermodiffusion.[25,26]

B. Boundary conditions

In the outlet of the burner nozzle, the temperature and mass flow of species are imposed. The velocity profile was obtained from a separate simulation of the flow in the nozzle, which tapers over a distance of 27.5 mm from a diameter of 3.9 mm to a diameter of 1.4 mm. The resulting velocity profile in the nozzle outlet could be fitted accurately by

$$v_z(r) = \frac{4}{3}\langle v \rangle \left(1 - \left(\frac{r}{R}\right)^6\right). \quad (2)$$

Here, $\langle v \rangle$ is the mean outlet velocity, r is the radial distance, and R is the inner radius of the burner outlet. The total flow was kept at 5.4 slm,[19] which corresponds to a mean velocity of $\langle v \rangle = 64$ m/s. The composition of the feed gas is based on the composition of a neutral oxy-acetylene flame, which in practice is a $47.5{:}52.5 = 0.9$ molar ratio of acetylene and oxygen.[19] The excess acetylene is defined as the fraction of acetylene that is fed in excess to that of a neutral flame. Thus, a 5% excess of acetylene ($Sac = 5\%$) corresponds to a feed gas composition of $48.72{:}51.28 = 0.95$ molar ratio of acetylene and oxygen. The acetylene bottle, in practice, contained about 1000 ppm of nitrogen. This was included in the simulations.

TABLE I. Settings used for the 2D simulations.

	Range	Standard value
Sac		5%
d	0.6–2.6 mm	0.6 mm
T	1200–1500 K	1400 K

Due to entrainment, there is a coflow of surrounding air, which is 300 K. This coflow could in principle be calculated self-consistently from the hydrodynamics model, by setting fixed pressure boundary conditions at all outlet boundaries. This, however, was found to lead to numerical instabilities. Therefore, a fixed inflow velocity was imposed on the boundary surrounding the nozzle. It was assumed that the coflow has a uniform velocity of 3 m/s when it enters the computational domain, corresponding to a total flowrate of 10 slm. This velocity is small compared to the gas velocities in the nozzle. It is therefore expected, that the imposed coflow does not significantly influence the flame hydrodynamics. Indeed, variations of the coflow velocity between 1 and 10 m/s showed that the flame shape and hydrodynamics were virtually insensitive to its exact value. Gradients perpendicular to the outlet plane are assumed to be zero, and there is no velocity component parallel to this plane. The walls are isothermal and no slip conditions are imposed. All walls were kept at 300 K, except for the substrate, which was set as indicated in Table I. As a result of species adsorption and desorption, there was a net flux of species toward or from the substrate, which led to a very small velocity component normal to this surface.

C. Discretization and numerical method

For the numerical solution of the model equations, we use our in-house CVD simulation code CVDMODEL.[26,27] This code has been applied successfully to the simulation of various thermal CVD processes,[1,27–29] as well as to the simulation of a steady-state atmospheric pressure methane–air flame.[30] For the latter, using the same gas-phase mechanism and transport properties, the flame length and thickness compared excellently to those simulated by Somers and de Goey.[7]

The model equations are discretized with the aid of the finite volume method.[31] A power-law differencing scheme is used for the spatial discretization of the diffusive and convective terms. The momentum-continuity coupling is accounted for through the SIMPLE pressure correction

scheme.[31] This leads to $(4+N)\times N_r\times N_z$ nonlinear, coupled algebraic equations for the two velocity components, the pressure correction, the temperature and the N gas species concentrations in each of the $N_r\times N_z$ grid points. When using first-order backward Euler time discretization, their general form is

$$\left(\sum_{\mathrm{nb}} a_{\phi,\mathrm{nb}} - S'_{\phi,P} + \frac{\rho}{\Delta t}\right)\phi_P = \sum_{\mathrm{nb}} a_{\phi,\mathrm{nb}}\phi_{\mathrm{nb}} + S^0_{\phi,P} + \frac{\rho}{\Delta t}\phi^*_P, \tag{3}$$

where a represents the discretization coefficients, and Δt the discretized time step. The subscripts P and nb refer to a particular grid point P and its four neighboring grid points, respectively, ϕ^*_P indicates the old value of ϕ_P, and the summations are taken over the neighboring grid cells.

The relatively short time scales on which the gas-phase reactions occur, make the set of equations to be solved stiff. The stability of the solution procedures for these equations can be improved by proper linearization of the source terms. The production rate of gas-phase species is added to the constant part S^0_ϕ, which is treated explicitly. The destruction rate of the gas-phase species, which usually is first order in the concentration, is included in the linearized part of the source term S'_ϕ, thus solving it implicitly. The source terms in the thermal-energy equation resulting from the reaction are linearized as recommended by Patankar.[31] Furthermore, false time-step underrelaxation is applied to achieve convergence,[31] i.e., in the iterative solution procedure toward the steady-state solution the time derivative is retained for numerical reasons only. Here, ϕ^*_P is the value of ϕ_P at the previous iteration, rather than at a previous time level. The value of the false time step is determined by the smallest time scale in the domain

$$\Delta t = \min_{i,P} \frac{c_{i,P}}{R^g_{i,P}}, \tag{4}$$

where $c_{i,P}$ is the concentration of species i at grid point P, and $R^g_{i,P}$ is the maximum of either the production or the destruction rate of species i. For this system, the value of the false time step is typically 0.1 μs. The relaxation of the other variables is carried out with an ordinary relaxation parameter. Furthermore, underrelaxation of the gas-phase properties is applied, since these are partly responsible for the coupling of the balance equations. The system can be solved using a tridiagonal-matrix algorithm. The coefficients for the species equations are calculated simultaneously to prevent dependence on the order of computation. As there is no carrier gas, all species equations are solved.

The fractional coverage θ_i of the surface species may be obtained from a set of ordinary differential equations

$$\frac{\partial\theta_i}{\partial t} = \frac{\sigma_i}{\eta}\sum_{k=1}^{K} \nu_{ik} R^s_k, \tag{5}$$

where η is the site density (mol/m^2), σ_i is the number of sites that a surface species occupies, ν_{ik} is the stoichiometric coefficient of the ith surface species in kth reaction, and R^s_k is the reaction rate of the kth reaction (mol/m^2 s). Unlike Eq. (1) for the gas-phase concentrations, Eq. (5) is an initial value problem that can be integrated over time to reach the stationary solution at $t\to\infty$ by means of an ordinary differential equation solver for stiff problems.[32,33]

Figure 1 depicts the grid on which most simulations are done. It has $N_r\times N_z = 61\times 149$ grid cells. In the radial direction the grid was the finest in the flame area. A cell at the flame front typically has a radial dimension of 17 μm. This is enough to ensure that the sharp temperature rise in the flame front is spanned by at least five grid cells, which has proved to be sufficient for methane–air flames.[30] In the axial direction, the typical grid size is 60 μm, which is refined near the substrate to 4 μm. Grid independence was checked by increasing the number of grid points by 50% in both directions to $N_r\times N_z = 92\times 225$ grid cells. This led to axial concentration profiles that were somewhat smoother at the flame front. Past the flame front, however, concentration differences between the standard grid and on the refined grid were less than 5% for all species.

D. Solution strategy

No accurate initial guess was needed for the solution procedure to converge. As an initial guess, all velocities were set to zero, except at the inlet boundary. The initial gas mixture composition corresponded to that of air in all grid points, except in the inlet boundary. To ignite the flame at startup, the temperature was set to 300 K, except for one grid point at the top of the inner corner of the burner pipe, which was set to $T = 2000$ K. As soon as the flame had ignited (i.e., after several hundreds of iterations), this fixed temperature point was removed.

Although the need for the use of very small false time steps resulted in a large number of iterations, stable, converged solutions of the full set of coupled model equations could nevertheless be readily obtained on relatively rough grids. On grids fine enough to accurately resolve the flame front, however, a fully coupled solution of the problem proved to be computationally prohibitive. Therefore, on these fine grids, we chose to simplify the problem by decoupling the detailed chemistry model from the flow and temperature simulations.

First, the flow and temperature field were calculated using a simple two-step reaction mechanism, consisting of one overall step from reactants to products and a second step in which hydrogen dissociation led to the necessary reduction of the flame temperature

$$\mathrm{C_2H_2 + O_2 \leftrightarrows 2CO + H_2}$$

$$k = 4\times 10^7 \exp\left(-\frac{8600}{T}\right)(\mathrm{m^3/(mol\times s)}), \tag{6}$$

$$\mathrm{2H + M \leftrightarrows H_2 + M} \quad k = 0.3\times 10^7 \times T^{-1}\,(\mathrm{m^3/(mol\times s)}). \tag{7}$$

The given rate constants are for the forward reactions. The reverse rate constants are calculated from the reaction thermodynamics. The one-dimensional temperature profiles, calculated with the premixed-flame unit of the CHEMKIN

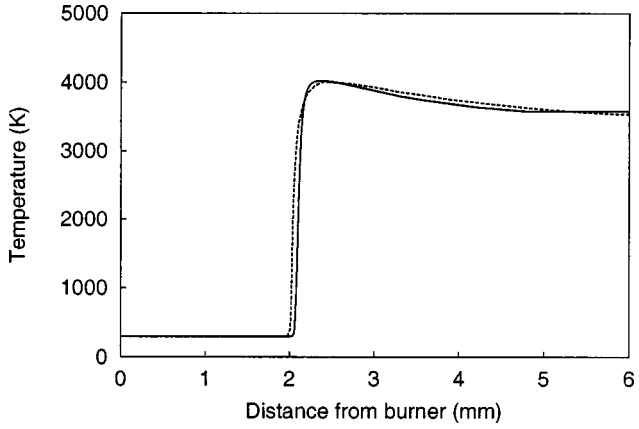

FIG. 2. Comparison between the temperature profile predicted by the detailed combustion mechanism (solid line), and the two-step mechanism (dotted line) in a one-dimensional free-burning premixed flame simulation, with the PREMIX code described in Ref. 34.

package,[34] are compared in Fig. 2 for full and two-step chemistry. This shows that the two-step chemistry accurately predicts the flame temperature profile, and therefore the velocity profiles.

The two-step model cannot, however, predict the concentrations of molecules and radicals leaving the flame front and causing diamond growth on the surface. Therefore, this two-step chemistry is only used to obtain the temperature and velocity profile in the flame. Subsequently, the species concentrations are calculated from the full chemistry model, using the temperature field from the two-step model. This allows for the use of large false time steps and, as a result, is computationally less demanding. In the major part of the flame, this approach is not expected to have a large influence on the results. However, in the zone where ambient air diffuses into the flame and reacts with the combustion products, there could be a temperature effect that is not accounted for by the two-step mechanism.

III. RESULTS

A. Validation of the model

To validate the oxy-acetylene flame simulations, radial and axial concentration profiles were compared to concentration profiles measured by Klein-Douwel *et al.*[19,35] with the aid of LIF. In LIF, a laser sheet of light of a certain wavelength is directed through the flame. Molecules are excited, and fall back to their normal state while emitting light. Light emitted perpendicularly to the flame is detected, thus providing a 2D concentration profile. However, only qualitative results are obtained, since an unknown fraction of the molecules falls back without emitting light, owing to collision with other molecules, i.e., quenching. The degree of quenching is, through the density, dependent on the temperature and on the type of molecules. Thus, care should be taken while interpreting LIF results in the presence of large temperature gradients, such as at the flame front and near the surface.

The shape of the simulated flame is indicated by the temperature profile and stream traces shown in Fig. 3. The model simulations correctly predict the experimentally observed cone-shaped flame with a length of about 7 mm and a flame–sheet thickness of about 0.2 mm. The flame reaches a maximum temperature of 3800 K directly behind the flame front. This maximum is well above the adiabatic flame temperature of 3300 K. This can be explained by the fact that, at the flame front, molecular hydrogen and water are formed in a supraequilibrium amount. Consequently, their radical atomic hydrogen is present in a subequilibrium amount. Since the dissociation of molecular into atomic hydrogen consumes heat, the temperature directly behind the flame front is higher than adiabatic. This phenomenon is referred to as temperature overshoot. In the zone behind the flame front,

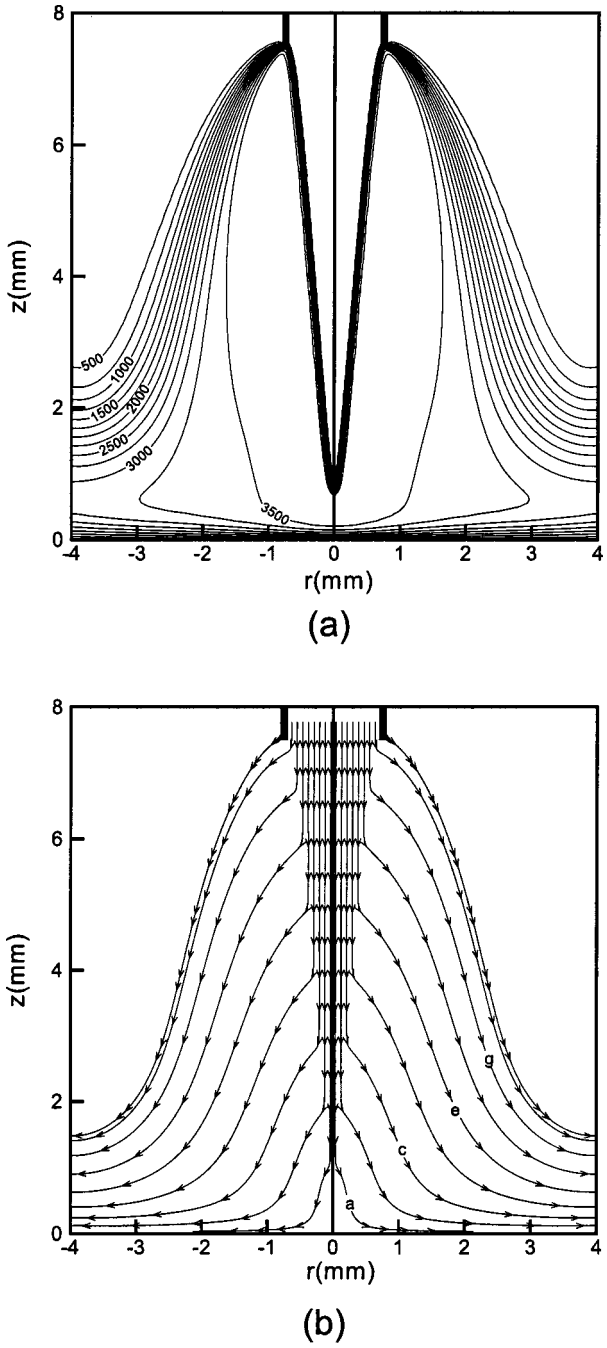

FIG. 3. Isotherms, marked in Kelvins (a) and stream traces (b) marked from a to g, in the oxy-acetylene torch reactor as predicted by the two-dimensional reactor model.

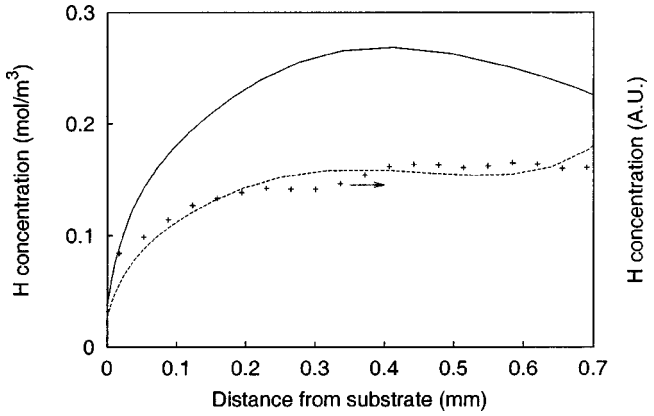

FIG. 4. Comparison between the atomic hydrogen profiles as predicted by stagnation flow calculations with the SPIN code, as described in Ref. 14, with $d=0.8$ mm, the 2D calculations with $d=0.6$ mm, and LIF experiments as presented in Ref. 35, with $d=0.85$ mm. The experimental values are in arbitrary units.

molecular hydrogen and water dissociate, and the temperature slowly decreases as a result. A more detailed discussion of this phenomenon can be found in Refs. 36, 15, and 37. Simulations for various values of the flame–tip-to-substrate distances d show similar temperature profiles: After the temperature maximum of 3800 K directly behind the flame front, the temperature slowly decreases to a temperature of about 3000 K at a few hundred microns from the surface. There, the temperature rapidly decreases to the substrate temperature of 1400 K. Thus, because the temperature changes relatively little between the flame front and a few hundred microns from the surface, LIF data in this region can be compared with simulations with some confidence.

In Fig. 4, the simulated axial atomic hydrogen profile is compared to the profile measured with LIF.[35] The concentration predicted by 1D stagnation flow simulations is also depicted. At this flame–tip-to-substrate distance, the 2D profile matches the measured profile well, despite the large temperature gradients between the flame–tip and the substrate. Evidently, the 2D simulations are in better qualitative agreement with experiments than the 1D simulations.

For various flame–tip-to-substrate distances, the simulated axial atomic hydrogen concentration profiles are shown in Fig. 5. Since the concentration is plotted, and not the mole fraction, the higher molecular density on the cold side of the flame front causes a peak in the concentration.

Regardless of the flame–tip-to-substrate distance, the profiles show two characteristics: First, as explained above, the H concentration increases slowly downstream from the flame front, to reach a maximum at a few hundred microns from the substrate. This maximum is higher as the flame–tip-to-substrate distance increases. Second, in a region within a few hundred microns from the substrate, the concentration decreases swiftly.

This second characteristic is also observed in measurements. Figure 5(b) shows that for all flame–tip-to-substrate distances, the experimental atomic hydrogen concentration decreases rapidly toward the substrate. It is not possible, however, to verify the first characteristic on the basis of these measurements. Only the experiments at a flame–tip-to-

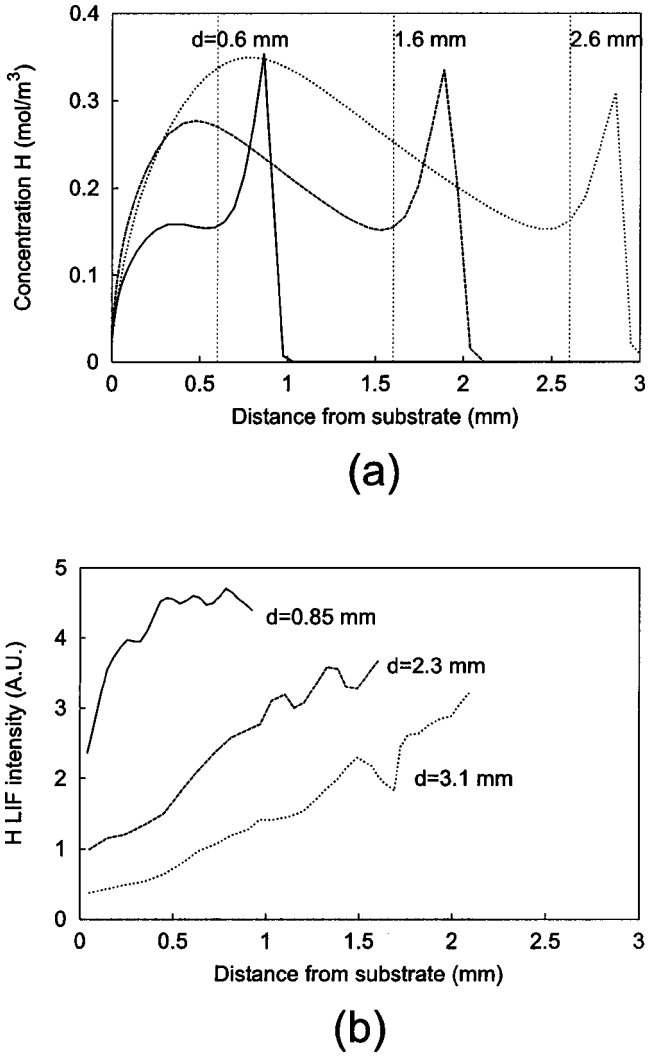

FIG. 5. Effect of the variation of the flame–tip-to-substrate distance on the simulated (a) and measured (b) axial atomic hydrogen profile. The latter have been taken from Ref. 35.

substrate distance $d=0.85$ mm cover the whole distance from the substrate to the flame tip. At this value of d, however, the increase in concentration behind the flame front is evident in neither the simulations nor the measurements. From 2D LIF pictures,[35] and in particular from their color reproductions in Ref. 38, however, it is clear that the maximum atomic hydrogen concentration lies some distance away from the flame front, in agreement with our simulations.

Opposed to the simulations, the measured atomic hydrogen LIF intensity at a fixed distance from the substrate decreases when d is increased. Moreover, the measurements indicate a much longer distance over which atomic hydrogen decreases in concentration. Two causes can be pointed out: (i) the different temperature profile near the substrate for different values of d, which makes comparison problematic and (ii) generation of atomic hydrogen, as predicted by the gas-phase reaction model, possibly is too slow. As a result, the simulated atomic hydrogen concentration does not reach its equilibrium value in the distance between the flame tip and the substrate. Consequently, if the flame–tip-to-substrate

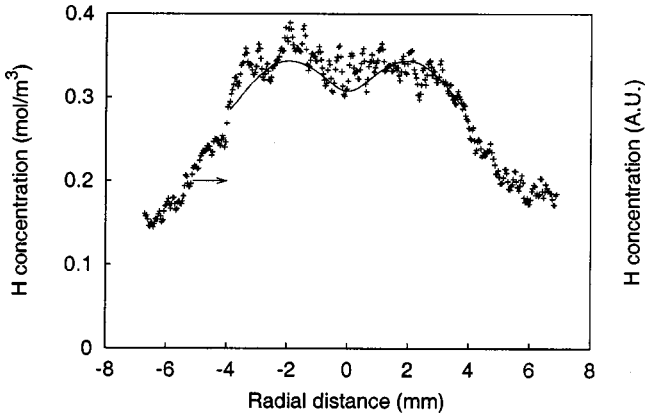

FIG. 6. Comparison between the radial atomic hydrogen profiles above the substrate as predicted by 2D calculations with $d=2.6$ mm, and LIF experiments, as described in Ref. 35, with $d=2.3$ mm. The experimental values are in arbitrary units.

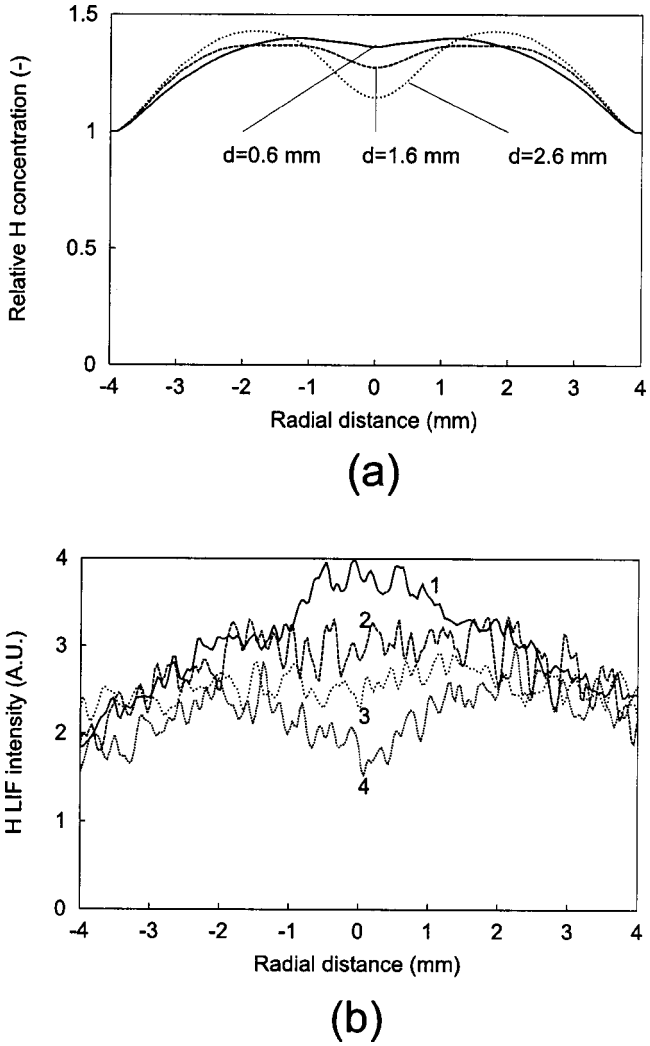

FIG. 7. Simulated (a) radial atomic hydrogen profiles directly above the surface, and profiles measured with LIF, as presented in Ref. 35 (b), both as a function of the flame–tip-to-substrate distance. The concentration is normalized with the concentration at $r=4$ mm which, in the case of the simulations, is 21.3 mmol/m^3 for $d=0.6$ mm, 23.7 mmol/m^3 for $d=1.6$ mm, and 22.2 mmol/m^3 for $d=2.6$ mm. The experimental curves correspond to (1) $d=0.85$ mm, (2) $d=1.68$ mm, (3) $d=2.3$ mm, and (4) $d=3.05$ mm.

distance is increased, higher maximum H concentrations are reached. At faster atomic hydrogen production rates, the H concentration reaches a maximum at a fixed distance from the flame front, and only decreases thereafter. This corresponds to the situation found in the measurements. The hypothesis of too slow a generation of atomic hydrogen in the gas phase chemistry model is further supported by the fact that the maximum in the atomic hydrogen concentration in 2D measurements is much closer to the flame front (0.7 mm)[38] than in the simulations (2 mm).

The radial atomic hydrogen profiles directly above the surface are compared with LIF measurements in Fig. 6. Good qualitative agreement is found between measurements and simulations. For both the simulations and the measurements, at larger d, Fig. 7 shows that there is a minimum in the concentration profile in the center that deepens with increasing flame–tip-to-substrate distance. Furthermore, the simulated peaks have about the same width as the measured peaks.

Figure 8 shows predicted 2D concentration distributions for C_2 and OH. C_2 is present at the flame front, and its concentration rapidly decreases away from the flame front. OH is present in a thin layer at the flame front and in the border area of the flame and the ambient air, the so-called ''lobes.'' All these predictions are in agreement with experimental observations.[19,35]

When comparing measured and predicted axial (Fig. 9) and radial (Fig. 10) C_2 concentration profiles, similar trends are observed: The width of the radial C_2 profile increases with increasing d, whereas the C_2 concentration at a fixed distance from the surface decreases with increasing d. However, the C_2 concentration decreases at a somewhat higher rate in the simulations than in experiments. Furthermore, comparison of Fig. 11 with 9 shows that the CH decomposition rate is slower than the C_2 decomposition rate in the simulations. This is not found in the measurements,[19] and it indicates that the degradation of carbon containing radicals is not predicted correctly. Another indication for this conclusion is that the decrease of the growth rate with increasing flame–tip-to-substrate distance is faster in the simulations than in experiments (see Fig. 12).

A quantitative validation was performed by comparing the simulation results to cavity ring down spectroscopy (CRDS) measurements of the CH concentration in the flame, as published by Stolk and ter Meulen.[39] In CRDS, absolute molecular densities integrated along the absorption path length are obtained. Measurements of CH[39] at 0.44 mm from the substrate, for flame–tip-to-substrate distances $d=1.08$ mm and $d=2.48$ mm, both yielded a value of 1×10^{16} m^{-2}. The simulations predict a value of 150×10^{16} m^{-2} for $d=0.6$ mm, which is a factor of 10^2 higher than the measurements, and a value of 1.16×10^{16} m^{-2} for $d=2.6$ mm, i.e., almost exactly the measured value. The overprediction of the CH concentration at short flame–tip-to-substrate distances again indicates that the gas-phase reaction mechanism predicts too low a CH decomposition rate.

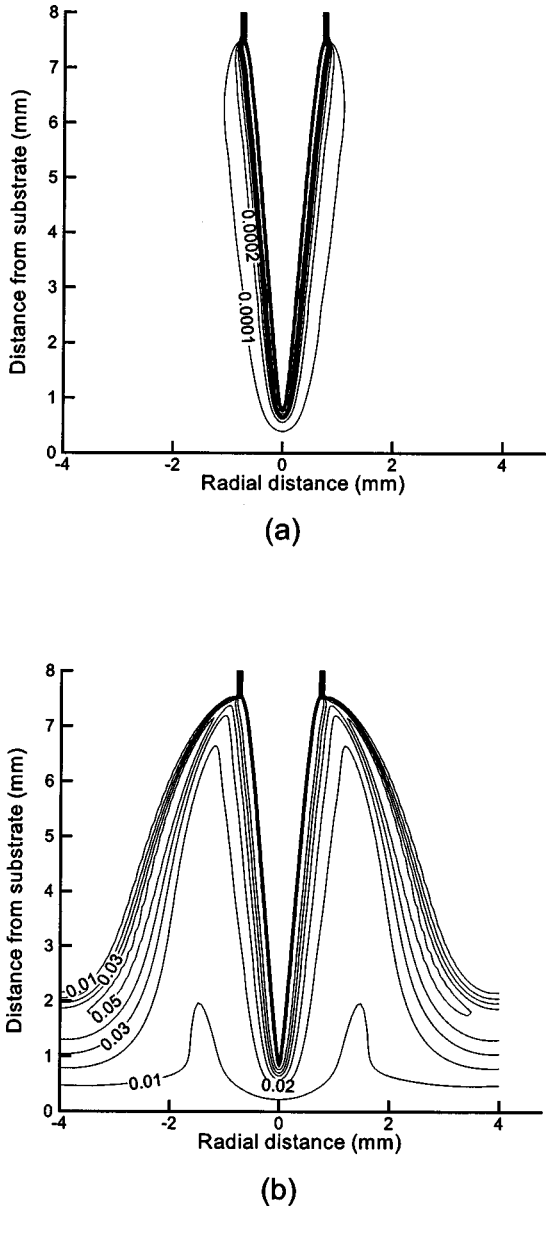

FIG. 8. Predicted C_2 (a) and OH (b) concentration profile (mol/m^3), $d = 0.6$ mm. The maximum C_2 concentration is 0.0011 mol/m^3.

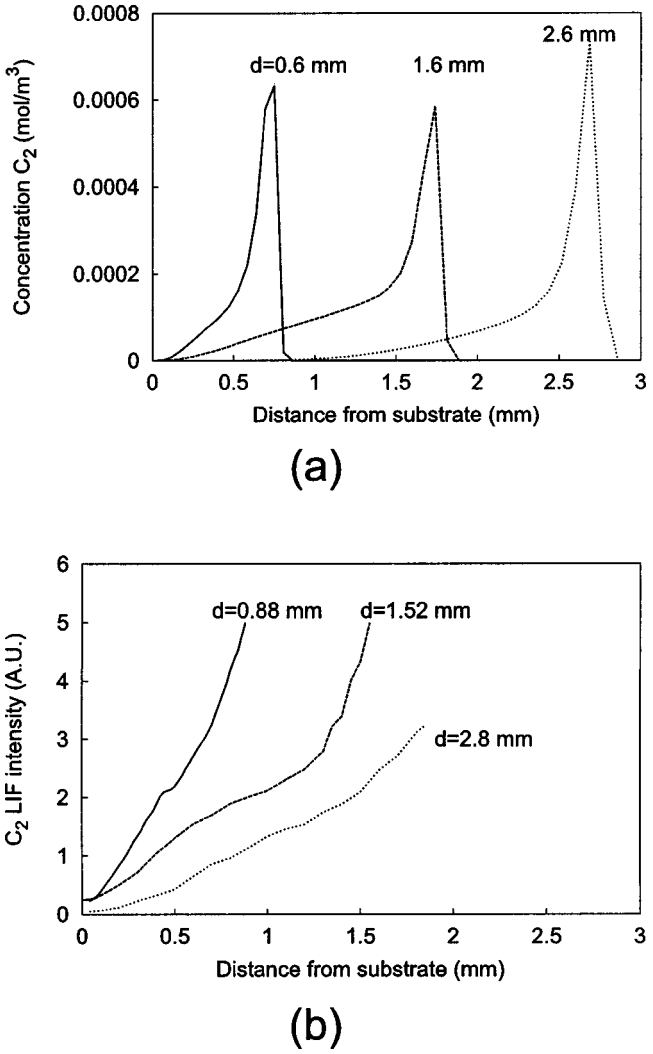

FIG. 9. Simulated (a) and measured (b) effect of variation of d on the C_2 concentration profile. Experimental data from Ref. 35. The experimental profiles for $d = 0.88$ mm and $d = 1.52$ mm are normalized to have the same maximum intensity. The profile for $d = 2.8$ mm is scaled arbitrarily as done by Klein-Douwel *et al.* (see Ref. 35).

Summarizing, the validation of the 2D gas-phase model shows that it correctly predicts the shape, length, and sheet thickness of the flame, as well as general trends in the reaction product concentrations. However, for the rich oxy-acetylene flames studied, the Miller–Melius combustion mechanism[12] appears to incorrectly predict the rate at which certain species, e.g., H, CH, and C_2, are produced or consumed behind the flame front. As a result, the predicted concentrations at specific locations in the reactor can be off by 1 or 2 orders of magnitude. Further study and optimization of the gas-phase mechanism for rich flames is necessary to improve the gas-phase predictions.

B. Regime characterization

Film-thickness profiles in oxy-acetylene flame CVD of diamond exhibit a striking similarity with radial mass-transfer profiles from jets impinging on a surface. As a result, the thought comes to mind that diamond film growth might well be determined by mass transfer limitations, rather than surface kinetics. This has consequences for the importance of hydrodynamic optimization of diamond CVD reactors: In the mass transfer limited regime, hydrodynamic optimization is of much greater importance than in the surface kinetics limited regime. To shed some light on this issue, we used our 2D flame simulations to determine the growth-limiting mechanisms in oxy-acetylene flame diamond CVD. This analysis is complicated by the fact that species concentrations are determined by the complex interaction of gas-phase reactions, surface reactions, and transport phenomena.

In the torch reactor, convection dominates diffusion outside a surface boundary layer, since local Péclet numbers are of the order $\mathrm{Pe} = O(100)$. Inside a thin boundary layer adjacent to the substrate, diffusion is the dominating species transport mechanism. The surface Damköhler number, which is the ratio between the characteristic time for diffusion through this boundary layer and the characteristic time for

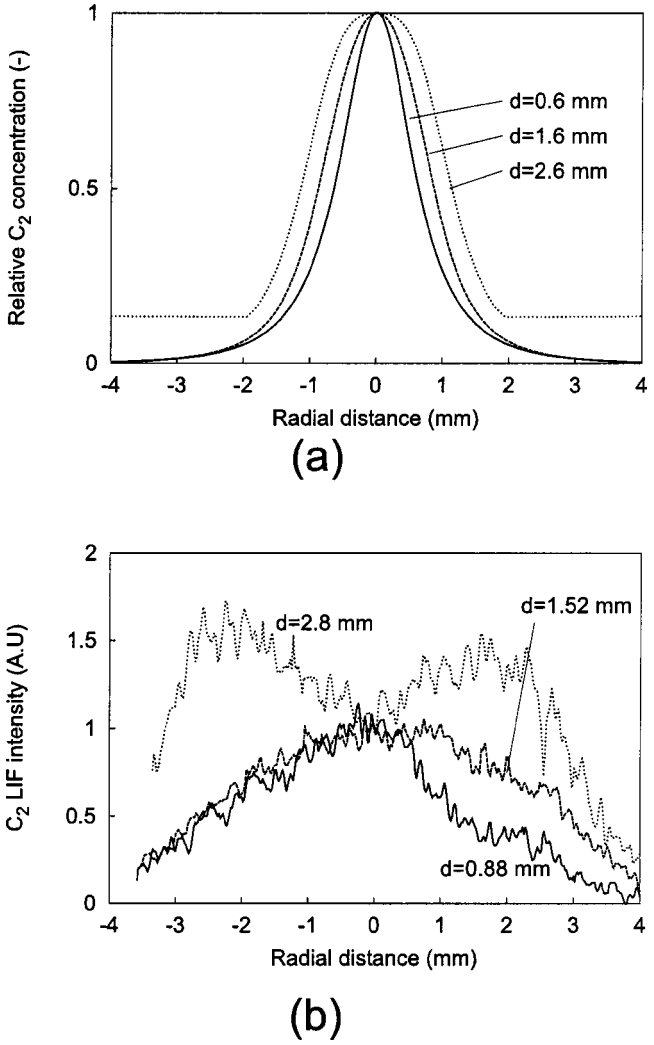

FIG. 10. Simulated (a) radial C_2 profiles directly above the surface and profiles measured with LIF (see Ref. 35) (b), as a function of the flame–tip-to-substrate distance. The concentration is normalized with the concentration at the center, which is 4.5×10^{-9} for $d=0.6$, 3.4×10^{-10} for $d=1.6$, and 6.2×10^{-14} for $d=2.6$. The latter is barely above the lower concentration limit.

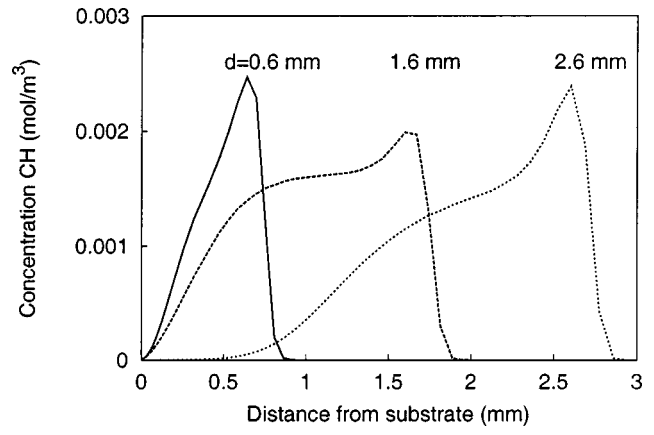

FIG. 11. Simulated effect of variation of d on the CH concentration profile.

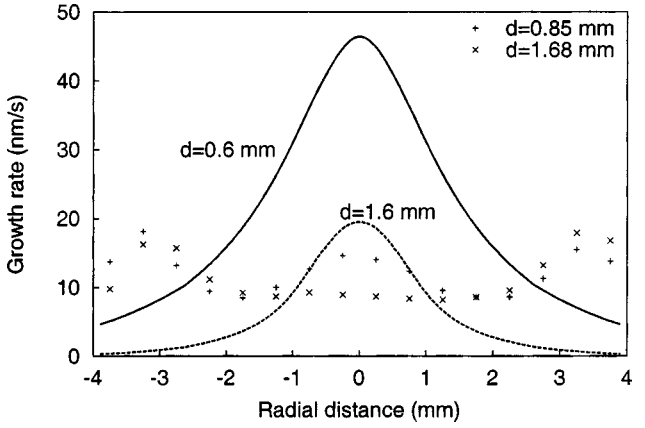

FIG. 12. Comparison between simulated (lines) and experimental (see Ref. 35) (points) growth rate at various flame–tip-to-substrate distances. Not depicted is the growth rate at $d=2.6$ mm, which is 0.1 nm/s at its maximum. The experimentally measured increase in growth rate at $r=3$ mm is ascribed to in-diffusion of nitrogen into the flame (see Ref. 42). Nitrogen is not included in the surface chemistry.

surface reactions,[40] determines the transition between transport-limited and kinetics-limited growth. The boundary layer thickness δ, estimated from the equation derived for stagnation flows,[41]

$$\frac{\delta}{d}=\frac{1}{\mathrm{Pe}}\exp\left(-\frac{\mathrm{Pe}}{2}\right)+\sqrt{\frac{\pi}{2\mathrm{Pe}}}\,\mathrm{erf}\left(\sqrt{\frac{\mathrm{Pe}}{2}}\right) \tag{8}$$

is on the order of 100 μm. The corresponding Damköhler number is smaller than 0.1 for all gaseous growth precursors. This indicates a kinetically controlled process. This observation is supported by a test where a 10% faster surface mechanism was implemented in the 2D simulations. If mass transfer limitations were of importance, this would lead to a less than 10% increase of the film growth rate. In agreement with the observation that the growth is fully controlled by surface kinetics, however, this modified surface reaction mechanism led to an almost exactly 10% higher growth rate over the entire substrate surface.

Outside the boundary layer, convection and homogeneous reaction dominate over diffusion. If diffusion were completely negligible, the composition evolution of a small gas volume moving along a stream trace could be transformed into the time evolution of an isolated, perfectly stirred, gas volume with identical initial composition. In Fig. 13(b), the CH_3 concentration integrated along four different stream traces is plotted. The four curves are almost identical, except for stream trace (a), which passes along the substrate. Figure 13(a) shows the time evolution of the CH_3 concentration integrated along the center line of the 2D flame. Also plotted is the time evolution of the CH_3 concentration as calculated for a perfectly stirred tank reactor. There is a striking similarity between the time evolution in a 0D stirred tank, and the time integration along stream traces in the 2D flame, both in the maximum value of the temperature and in the widths of the temperature peak. The latter, however, is approximately 50% larger in the 2D simulations, indicating a minor effect of diffusion. Similar observations were made

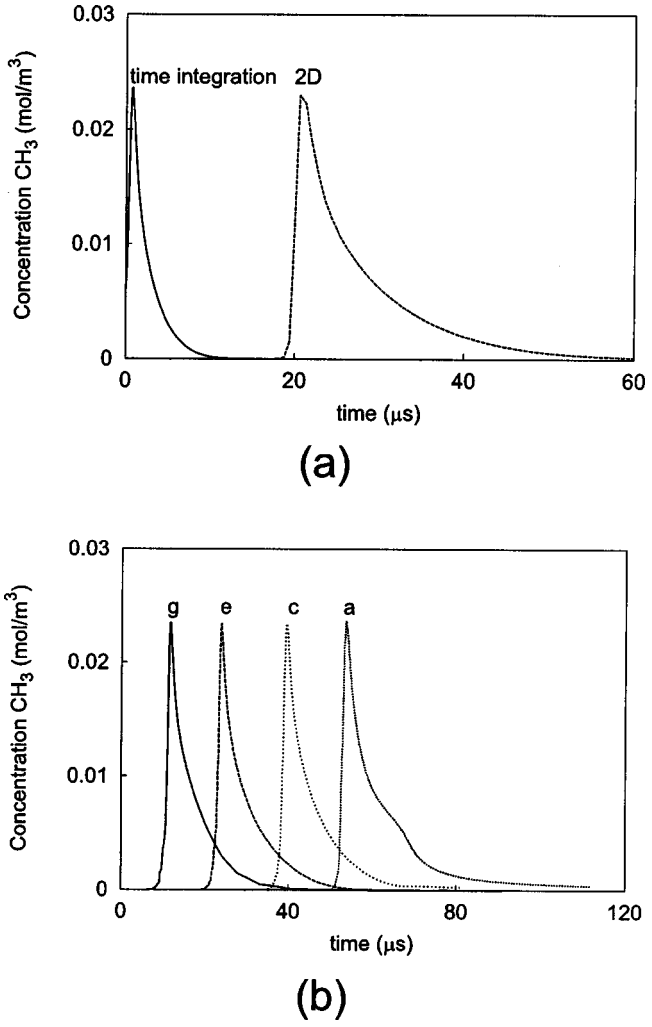

FIG. 13. Development of the CH_3 concentration over time in the case of a time integration both along the center of a 2D premixed flame ($d = 2.6$ mm) (a) and along stream traces in the 2D simulation. The initial conditions of the time integration were the same as those in a 1D premixed flame reactor at the point where the temperature is 2000 K. The curves in (b) represent the concentration along stream traces g, e, c, and a, respectively, depicted in Fig. 3.

for the other hydrocarbon radical species, where the relative importance of diffusion was found to further decrease with increasing molecular size, i.e., with decreasing diffusivity. This indicates that diffusion is of minor importance compared to convection for the transport of hydrocarbons outside the substrate boundary layer. Similar comparisons showed that this is not the case for atomic hydrogen, the diffusion of which causes flame propagation. It has a much larger diffusivity than hydrocarbon species and its diffusion plays a significant role in smearing out the H concentration profiles.

To compare the relative importance of reaction and convection behind the flame front, the following should be considered: If convection were much faster than reaction, constant concentration profiles would be found between the flame front and the substrate, which is obviously not the case. If reactions were much faster than convection, the mixture would be close to local equilibrium everywhere. At postflame conditions we found that the gas mixture is far from its equilibrium state; hydrocarbon radical concentrations are 5 orders of magnitude higher than in equilibrium. Thus, both the gas-phase reactions and convection play an important role in the region between the flame front and the substrate boundary layer.

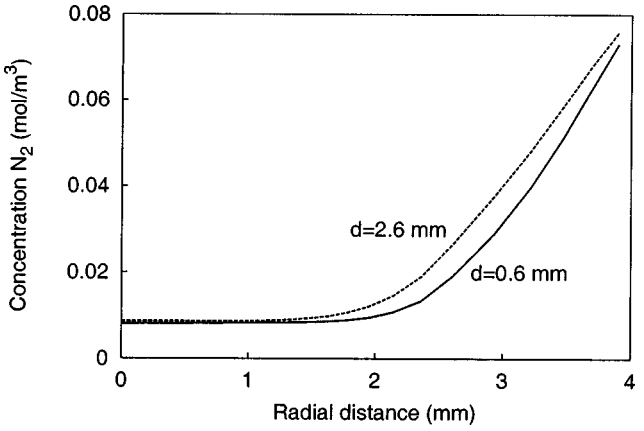

FIG. 14. Effect of the variation in flame–tip-to-substrate distance on the radial nitrogen concentration above the diamond substrate.

C. Nitrogen in-diffusion

Experimentally,[42] a central region of uniform good quality diamond growth is found to be limited by an annulus of enhanced growth, which starts 2 mm from the center. The diamond deposited in this annulus displays amorphous features. The presence of this annulus is attributed to in-diffusion of nitrogen into the flame.[42] Here, this hypothesis is tested against our 2D simulations. To this end, nitrogen is included in the simulations as an inert species. As in the experiments, a small amount of nitrogen, i.e., 1000 ppm, is present in the feed gas, whereas the coflow of ambient air consists of 80% nitrogen. Simulated radial nitrogen concentration profiles directly above the surface are shown in Fig. 14. It shows that the concentration above the center is equal to that in the feed. From 2 mm onwards, nitrogen from the ambient air is present. Nitrogen, or a nitrogen containing species, could thus very well be responsible for the observed annular region of enhanced growth.

Experiments[35] also showed that the diamond growth rate in the central region of the substrate changes with the flame–tip-to-substrate distance d. Since it is known that nitrogen in the gas phase causes an increased film growth rate, the growth rate in the central region may be influenced by an increase in nitrogen contamination of the gas owing to increased in-diffusion of nitrogen gas from the ambient air. Figure 14, however, shows that when d is increased, the nitrogen concentration above the central region of the diamond surface does not change significantly. Apparently, in-diffusion of nitrogen is not strongly dependent on the flame–tip-to-substrate distance. This is possibly because in-diffusion takes place over the entire nozzle-to-substrate length, which does not vary much when d is increased.

D. Variation of substrate temperature

The influence of the substrate temperature on the diamond growth was studied for the ranges of process condi-

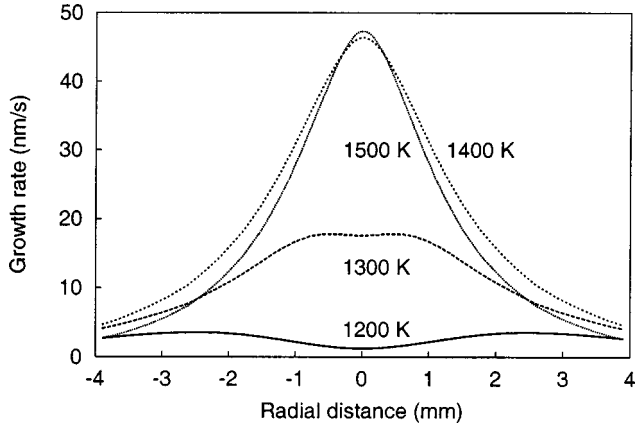

FIG. 15. Effect of the variation in substrate temperature on the growth rate of diamond.

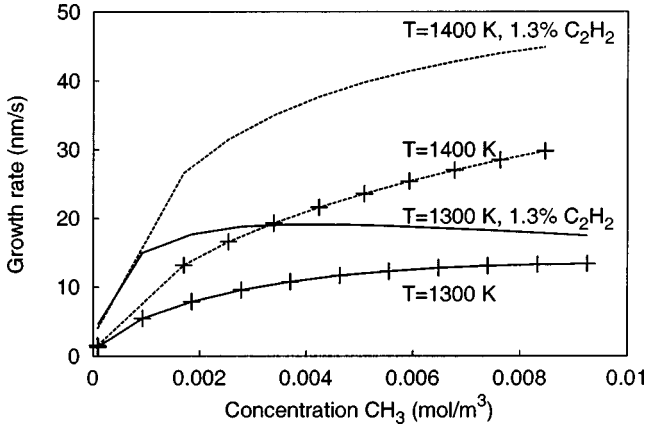

FIG. 16. Intrinsic study of the effect of the variation in gas-phase CH_3 concentration and surface temperature on the diamond growth rate. The data were obtained from a perfectly stirred tank reactor simulation under the conditions specified in Table II.

tions specified in Table I. Figure 15 shows the influence of the surface temperature on the diamond growth rate. It increases with the temperature until 1400 K. This was already observed in our 1D simulations.[14,15] What attracts attention is that at lower surface temperatures, growth at the center levels off, or even shows a minimum. A center of constant growth rate is also found experimentally.[43] This flat center is all the more noteworthy since CH_3, the main carbon source of diamond, exhibits a distinct maximum above the center. Using a simple first-order dependence of the growth rate on the CH_3 concentration as, e.g., proposed by Goodwin,[44] would thus lead to a maximum growth rate in the center.

To be able to explain this behavior, 0-D, perfectly stirred reactor simulations[23] were performed under the conditions shown in Fig. 16 (see Table II). In these simulations, the atomic and molecular hydrogen and methyl radical concentrations were set equal to the concentrations directly above the surface as predicted by the 2D simulation. Figure 16 shows the dependence of the growth rate on the CH_3 concentration. In our growth model, it has a first-order dependency of the growth rate on the CH_3 concentration at lower concentrations.[14] Under these conditions, the reaction steps that follow the initial adsorption of CH_3 are fast. At higher CH_3 concentrations, however, the growth rate levels off. This effect is more noticeable at lower temperatures. At these high CH_3 concentrations, the surface reactions are no longer fast enough to transform the adsorbed carbon into diamond, and thus the number of sites available for CH_3 adsorption decreases. A surface reaction with an activation energy, the so-called beta-scission reaction, becomes limiting.

TABLE II. Gas-phase composition applied in the surface kinetics simulations with the aid of a perfectly stirred tank reactor in Fig. 16. Temperatures of 1300 and 1400 K were applied, and the pressure was 10^5 Pa.

Species	Mole fraction
CH_3	1×10^{-5}–1×10^{-3}
C_2H_2	$0/1.3\times10^{-2}$
H	3.7×10^{-3}
H_2	0.256
CO	Remainder

This, however, does not explain the minimum in the growth at the center at a temperature of 1200 K. The simulations were repeated in the presence of 1.3% acetylene, i.e., the acetylene concentration at the center predicted by the 2D simulation. Figure 16 demonstrates that the growth rate now even decreases at higher CH_3 concentrations for lower substrate temperatures. This is caused by acetylene, which contributes significantly to the growth at these concentrations. If the CH_3 concentration is increased, the reduction of the number of free sites hinders the adsorption of acetylene. This results in a decrease in the adsorption of acetylene and in the growth rate. Figure 16 shows that, either with or without the presence of acetylene, a temperature that is too high is not beneficial for the growth of a flat diamond layer.

IV. CONCLUSIONS

We presented 2D simulations of the hydrodynamics and detailed chemistry in oxy-acetylene flames for diamond CVD.

Comparison to LIF experiments shows that certain trends are predicted correctly by the model. An increase in the flame–tip-to-substrate distance leads to a deepening of the minimum in the atomic hydrogen concentration profile above the center of the substrate, and a widening of the C_2 profile in both experiment and simulation. Other predictions were less accurate, viz. the position of the atomic hydrogen maximum in the reactor and the degradation rate of C_2 and CH. The cause of these discrepancies is likely to be found in the application of the Miller–Melius hydrocarbon combustion mechanism to rich oxy-acetylene flames. We suggest that the predicted production rate of atomic hydrogen is too low, resulting in a temperature overshoot that is too large.

Nevertheless, several conclusions can be drawn from the simulations concerning fundamental mechanisms in oxy-acetylene diamond CVD. Compared to diffusion in the boundary layer near the substrate, the deposition chemistry is slow and thus rate-determining. In the flame and postflame region, diffusion plays a minor role compared to homogeneous chemistry and convection. Atomic hydrogen is an im-

portant exception. Exemplary in this respect is the fact that the flame propagates because of upstream diffusion of atomic hydrogen. To describe the atomic hydrogen profiles correctly, thermodiffusion must be included in the simulations.

Simulations show that nitrogen penetration from the ambient air into the flame is hardly affected by the flame–tip-to-substrate distance. Thus, in-diffusion of nitrogen cannot explain the experimentally observed effect on the diamond growth rate of a change in flame–tip-to-substrate distance. Nitrogen in-diffusion, however, is likely to be responsible for the observed annulus of enhanced growth.

It was also shown that the growth of the diamond layer is not proportional to the concentration of the main gas-phase precursor CH_3 above the surface. The diamond layer is much flatter than would be expected from the distribution of this species. The reason for this can be found in the surface kinetics. At higher CH_3 concentrations, the growth rate levels off, since surface reaction steps become limiting. This results in fewer sites available for adsorption. Finally, the complex interaction between the CH_3 and C_2H_2 precursors was shown. Their combined effect on the diamond growth is not the simple addition of their separate growth contributions. Addition of acetylene to the reaction mixture above the substrate in large amounts relative to CH_3, leads to a small minimum in growth at the center. At high acetylene concentrations, acetylene contributes significantly to diamond growth. A high CH_3 concentration, however, reduces the number of sites available for the adsorption of acetylene. Combined with the zeroth order dependence of the growth rate on the CH_3 concentration, this results in a decrease of the growth rate.

ACKNOWLEDGMENTS

The authors would like to thank Robert Klein-Douwel and Hans ter Meulen for the use of their experimental data and for many stimulating discussions.

[1] K. J. Kuijlaars, C. R. Kleijn, and H. E. A. van den Akker, Solid-State Electron. **42**, A43 (1998).
[2] R. Rota, F. Bonini, A. Servida, M. Morbidelli, and S. Carà, Chem. Eng. Sci. **49**, 4211 (1995).
[3] C. A. Wolden, Z. Sitar, and J. T. Prater (unpublished).
[4] B. A. V. Bennett and M. D. Smooke, Combust. Theory Modell. **2**, 221 (1998).
[5] H. C. de Lange and L. P. H. de Goey, Combust. Sci. Technol. **92**, 423 (1993).
[6] H. C. de Lange and L. P. H. de Goey, Int. J. Numer. Methods Eng. **37**, 497 (1994).
[7] L. M. T. Somers and L. P. H. de Goey, Combust. Sci. Technol. **37**, 497 (1994).
[8] X. Zhou, G Brenner, F. Weber, and F Durst, Int. J. Heat Mass Transf. **42**, 1757 (1999).
[9] A. Ern and V. Giovangigli, Combust. Theory Modell. **2**, 349 (1998).
[10] *Reduced Kinetic Mechanisms and Asymptotic Approximations for Methane–Air Flames, Lecture Notes in Physics*, edited by M. D. Smooke (Springer, Berlin, 1991).
[11] G. Tsataronis, Brennst.-Waerme-Kraft **78**, 249 (1978).
[12] J. A. Miller and C. F. Melius, Combust. Flame **91**, 21 (1992).
[13] E. Meeks, R. J. Kee, D. S. Dandy, and M. E. Coltrin, Combust. Flame **92**, 144 (1992).
[14] M. Okkerse, M. H. J. M. de Croon, C. R. Kleijn, G. B. Marin, and H. E. A. van den Akker, J. Appl. Phys. **84**, 6387 (1998).
[15] M. Okkerse, M. H. J. M. de Croon, C. R. Kleijn, G. B. Marin, and H. E. A. v. d. Akker, in *Fundamental gas-phase and surface chemistry of vapor-phase materials synthesis*, edited by M. D. Allendorf, M. R. Zachariah, L. Mountziaris, and A. H. McDaniel (Electrochemical Society, Pennington, NJ, 1998), p. 293.
[16] C. C. Battaile, D. J. Srlolovitz, and J. E. Butler, J. Appl. Phys. **82**, 6293 (1997).
[17] C. C. Battaile, D. J. Srlolovitz, and J. E. Butler, J. Cryst. Growth **194**, 353 (1998).
[18] M. Grujicic and S. G. Lai, J. Mater. Sci. **34**, 7 (1999).
[19] R. J. H. Klein-Douwel, J. J. L. Spaanjaars, and J. J. ter Meulen, J. Appl. Phys. **78**, 2086 (1995).
[20] R. B. Bird, W. E. Stewart, and E. N. Lightfood, *Transport Phenomena* (Wiley, New York, 1960).
[21] J. O. Hirschfelder, C. F. Curtiss, and R. B. Bird, *Molecular Theory of Gases and Liquids* (Wiley, New York, 1967).
[22] R. C. Reid and T. K. Sherwood, *The Properties of Gases and Liquids*, 2nd ed. (McGraw–Hill, New York, 1966).
[23] R. J. Kee, F. M. Rupley, and J. A. Miller, Technical Report No. SAND89-8009B.UC-706, SANDIA National Laboratories, Albuquerque, NM (unpublished).
[24] C. R. Wilke, Chem. Eng. Prog. **46**, 95 (1950).
[25] R. Clark Jones, Phys. Rev. **59**, 1019 (1941).
[26] C. R. Kleijn and Ch. Werner, *Modeling of Chemical Vapor Deposition of Tungsten Films* (Birkhäuser, Basel, 1993).
[27] C. R. Kleijn, J. Electrochem. Soc. **138**, 2190 (1991).
[28] C. R. Kleijn and C. J. Hoogendoorn, Chem. Eng. Sci. **46**, 321 (1991).
[29] C. R. Kleijn, C. J. Hoogendoorn, A. Hasper, J. Holleman, and J. Middelhoek, J. Electrochem. Soc. **138**, 509 (1991).
[30] C. R. Kleijn, M. Okkerse, and H. E. A. VandenAkker, in *Computational Technologies for Fluid/Thermal/Structural Chemical Systems with Industrial Applications*, edited by V. V. Kudriavtsev and C. R. Kleijn (ASME, New York, 1999), pp. 219–226.
[31] S. V. Patankar, *Numerical Heat Transfer and Fluid Flow* (Hemisphere, Washington DC, 1980).
[32] P. N. Brown, G. D. Byrne, and A. C. Hindmarsch, SIAM (Soc. Ind. Appl. Math.) J. Sci. Stat. Comput. **10**, 1038 (1989).
[33] A. C. Hindmarsch, in *Scientific Computing*, edited by R. Stepleman (North–Holland, Amsterdam, 1983), pp. 55–64.
[34] R. J. Kee, J. F. Grcar, M. D. Smooke, and J. A. Miller, A fortran program for modeling steady laminar one-dimensional premixed flames, Sandia National Laboratories, (1988).
[35] R. J. H. Klein-Douwel and J. J. ter Meulen, J. Appl. Phys. **83**, 4734 (1998).
[36] E. Meeks, R. J. Kee, D. S. Dandy, and M. E. Coltrin, Combust. Flame **92**, 144 (1993).
[37] C. Wolden, K. K. Gleason, and J. B. Howard, Combust. Flame **96**, 75 (1994).
[38] R. J. H. Klein-Douwel and J. J. ter Meulen (personal communication).
[39] R. L. Stolk and J. J. ter Meulen, Diamond Relat. Mater. **8**, 1251 (1999).
[40] K. F. Jensen, in *Chemical Vapor Deposition-Principles and Applications*, edited by M. L. Hitchman and K. F. Jensen (Academic, London, 1993), pp. 31–90.
[41] K. J. Kuijlaars, Ph.D. thesis, Delft University of Technology, The Netherlands, 1996.
[42] R. J. H. Klein-Douwel, J. J. Schermer, and J. J. ter Meulen, Diamond Relat. Mater. **7**, 1118 (1998).
[43] G. Janssen, Ph.D. thesis, Katholieke Universiteit Nıjmegen, The Netherlands, 1994.
[44] D. G. Goodwin, J. Appl. Phys. **74**, 6888 (1993).